SUPPLEMENTARY INFORMATION

Full-Length $G\alpha_q$–Phospholipase C-β3 Structure Reveals Interfaces of the C-terminal Coiled-Coil Domain

Angeline M. Lyon, Somnath Dutta, Cassandra A. Boguth, Georgios Skiniotis, and John J. G. Tesmer

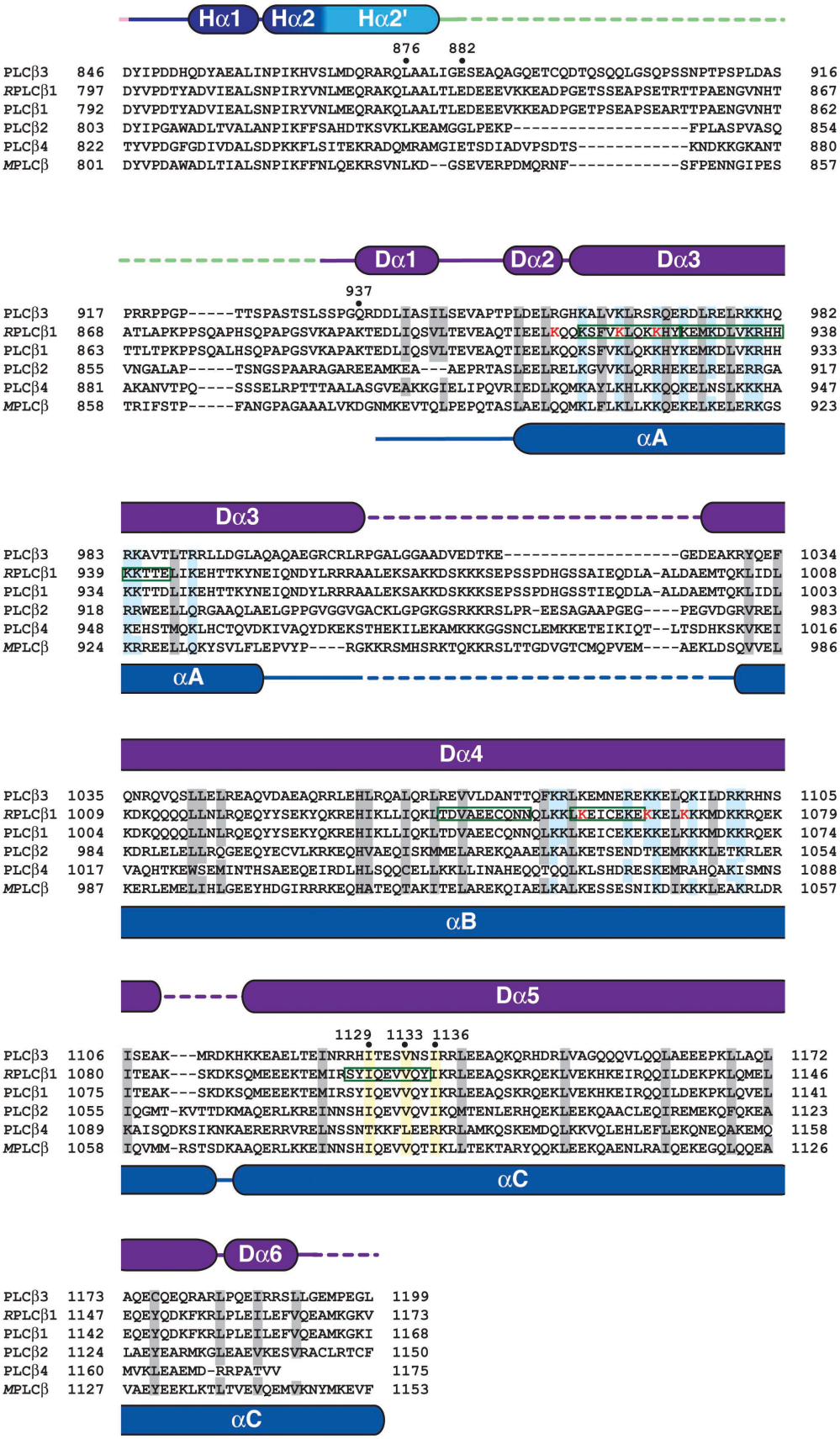
Hα1
Hα2
Hα2'
876
882
PLCβ3 846 DYIPDDHQDYAEALINPIKHVSLMDQRARQLAALIGESEAQAGQETCQDTQSQQLGSQPSSNPTPSPLDAS 916
RPLCβ1 797 DYVPDTYADVIEALSNPIRYVNLMEQRAKQLAALTLEDEEEVKKEADPGETSSEAPSETRTTPAENGVNHT 867
PLCβ1 792 DYVPDTYADVIEALSNPIRYVNLMEQRAKQLAALTLEDEEEVKKEADPGETPSEAPSEARTTPAENGVNHT 862
PLCβ2 803 DYIPGAWADLTVALANPIKFFSAHDTKSVKLKEAMGGLPEKP----------FPLASPVASQ 854
PLCβ4 822 TYVPDGFGDIVDALSDPKKFLSITEKRADQMRAMGIETSDIADVPSDTS----------KNDKKGKANT 880
MPLCβ 801 DYVPDAWADLTIALSNPIKFFNLQEKRSVNLKD--GSEVERPDMQRNF----------SFPENNGIPES 857
Dα1
Dα2
Dα3
937
PLCβ3 917 PRRPPGP-----TTSPASTSLSSPGQRDDLIASILSEVAPTPLDELRGHKALVKLRSRQERDLRELRKKHQ 982
RPLCβ1 868 ATLAPKPPSQAPHSQPAPGSVKAPAKTEDLIQSVLTEVEAQTIEELKQQKSFVKLQKKHYKEMKDLVKRHH 938
PLCβ1 863 TTLTPKPPSQALHSQPAPGSVKAPAKTEDLIQSVLTEVEAQTIEELKQQKSFVKLQKKHYKEMKDLVKRHH 933
PLCβ2 855 VNGALAP-----TSNGSPAARAGAREEAMKEA---AEPRTASLEELRELKGVVKLQRRHEKELRELERRGA 917
PLCβ4 881 AKANVTPQ----SSSELRPTTTAALASGVEAKKGIELIPQVRIEDLKQMKAYLKHLKKQQKELNSLKKKHA 947
MPLCβ 858 TRIFSTP-----FANGPAGAAALVKDGNMKEVTQLPEPQTASLAELQQMKLFLKLLKKQEKELKELERKGS 923
αA
Dα3
PLCβ3 983 RKAVTLTRRLLDGLAQAQAEGRCRLRPGALGGAADVEDTKE----------GEDEAKRYQEF 1034
RPLCβ1 939 KKTTELIKEHTTKYNEIQNDYLRRRAALEKSAKKDSKKKSEPSSPDHGSSAIEQDLA-ALDAEMTQKLIDL 1008
PLCβ1 934 KKTTDLIKEHTTKYNEIQNDYLRRRAALEKSAKKDSKKKSEPSSPDHGSSTIEQDLA-ALDAEMTQKLIDL 1003
PLCβ2 918 RRWEELLQRGAAQLAELGPPGVGGVGACKLGPGKGSRKKRSLPR-EESAGAAPGEG----PEGVDGRVREL 983
PLCβ4 948 KEHSTMQKLHCTQVDKIVAQYDKEKSTHEKILEKAMKKKGGSNCLEMKKETEIKIQT--LTSDHKSKVKEI 1016
MPLCβ 924 KRREELLQKYSVLFLEPVYP----RGKKRSMHSRKTQKKRSLTTGDVGTCMQPVEM----AEKLDSQVVEL 986
αA
Dα4
PLCβ3 1035 QNRQVQSLLELREAQVDAEAQRRLEHLRQALQRLREVVLDANTTQFKRLKEMNEREKKELQKILDRKRHNS 1105
RPLCβ1 1009 KDKQQQQLLNLRQEQYYSEKYQKREHIKLLIQKLTDVAEECQNNQLKKLKEICEKEKKELKKKMDKKRQEK 1079
PLCβ1 1004 KDKQQQQLLNLRQEQYYSEKYQKREHIKLLIQKLTDVAEECQNNQLKKLKEICEKEKKELKKKMDKKRQEK 1074
PLCβ2 984 KDRLELELLRQGEEQYECVLKRKEQHVAEQISKMMELAREKQAAELKALKETSENDTKEMKKKLETKRLER 1054
PLCβ4 1017 VAQHTKEWSEMINTHSAEEQEIRDLHLSQQCELLKKLLINAHEQQTQQLKLSHDRESKEMRAHQAKISMNS 1088
MPLCβ 987 KERLEMELIHLGEEYHDGIRRRKEQHATEQTAKITELAREKQIAELKALKESSESNIKDIKKKLEAKRLDR 1057
αB
Dα5
1129
1133
1136
PLCβ3 1106 ISEAK---MRDKHKKEAELTEINRRHITESVNSIRRLEEAQKQRHDRLVAGQQQVLQQLAEEEPKLLAQL 1172
RPLCβ1 1080 ITEAK---SKDKSQMEEEKTEMIRSYIQEVVQYIKRLEEAQSKRQEKLVEKHKEIRQQILDEKPKLQMEL 1146
PLCβ1 1075 ITEAK---SKDKSQMEEEKTEMIRSYIQEVVQYIKRLEEAQSKRQEKLVEKHKEIRQQILDEKPKLQVEL 1141
PLCβ2 1055 IQGMT-KVTTDKMAQERLKREINNSHIQEVVQVIKQMTENLERHQEKLEEKQAACLEQIREMEKQFQKEA 1123
PLCβ4 1089 KAISQDKSIKNKAERERRVRELNSSNTKKFLEERKRLAMKQSKEMDQLKKVQLEHLEFLEKQNEQAKEMQ 1158
MPLCβ 1058 IQVMM-RSTSDKAAQERLKKEINNSHIQEVVQTIKLLTEKTARYQQKLEEKQAENLRAIQEKEGQLQQEA 1126
αC
Dα6
PLCβ3 1173 AQECQEQRARLPQEIRRSLLGEMPEGL 1199
RPLCβ1 1147 EQEYQDKFKRLPLEILEFVQEAMKGKV 1173
PLCβ1 1142 EQEYQDKFKRLPLEILEFVQEAMKGKI 1168
PLCβ2 1124 LAEYEARMKGLEAEVKESVRACLRTCF 1150
PLCβ4 1160 MVKLEAEMD-RRPATVV 1175
MPLCβ 1127 VAEYEEKLKTLTVEVQEMVKNYMKEVF 1153
αC

Supplementary Figure 1. Sequence alignment and conservation of CTDs from PLCβ isozymes. Secondary structure of the distal CTDs from human PLCβ3 and turkey PLCβ (from PDB entry 1JAD[26]) are shown above and below the primary sequence, respectively, with rounded rectangles representing helices, and dashed lines indicating disordered regions in PLCβ3 or engineered deletions in turkey. Residues that were mutated in this study, or that mark the ends of the CTD linker deletion, are denoted by black circles with the corresponding residue number for PLCβ3 above the alignment. Gray boxes indicate conserved hydrophobic residues. Light blue boxes indicate the conserved basic residues that form the basic ridge proposed to interact with membranes. Yellow boxes indicate the conserved hydrophobic patch. Residues colored red are those mutated by Kim *et al* that impaired $G\alpha_q$-dependent activation and particulate association[21]. Residues boxed in green are tracts mutated by Ilkaeva *et al* that impaired $G\alpha_q$-dependent activation and GAP activity[27]. Species and Genbank entry numbers for the sequences are as follows: PLCβ3 (*H. sapiens* PLCβ3, NM_000932), *R*PLCβ1 (*R. norvegicus* PLCβ1, NP_001071109), PLCβ1 (*H. sapiens* PLCβ1, AAF86613), PLCβ2 (*H. sapiens* PLCβ2, NP_004564), PLCβ4 (*H. sapiens* PLCβ4, AAI17459), and *M*PLCβ (*M. gallopavo* PLCβ, AAC60011).

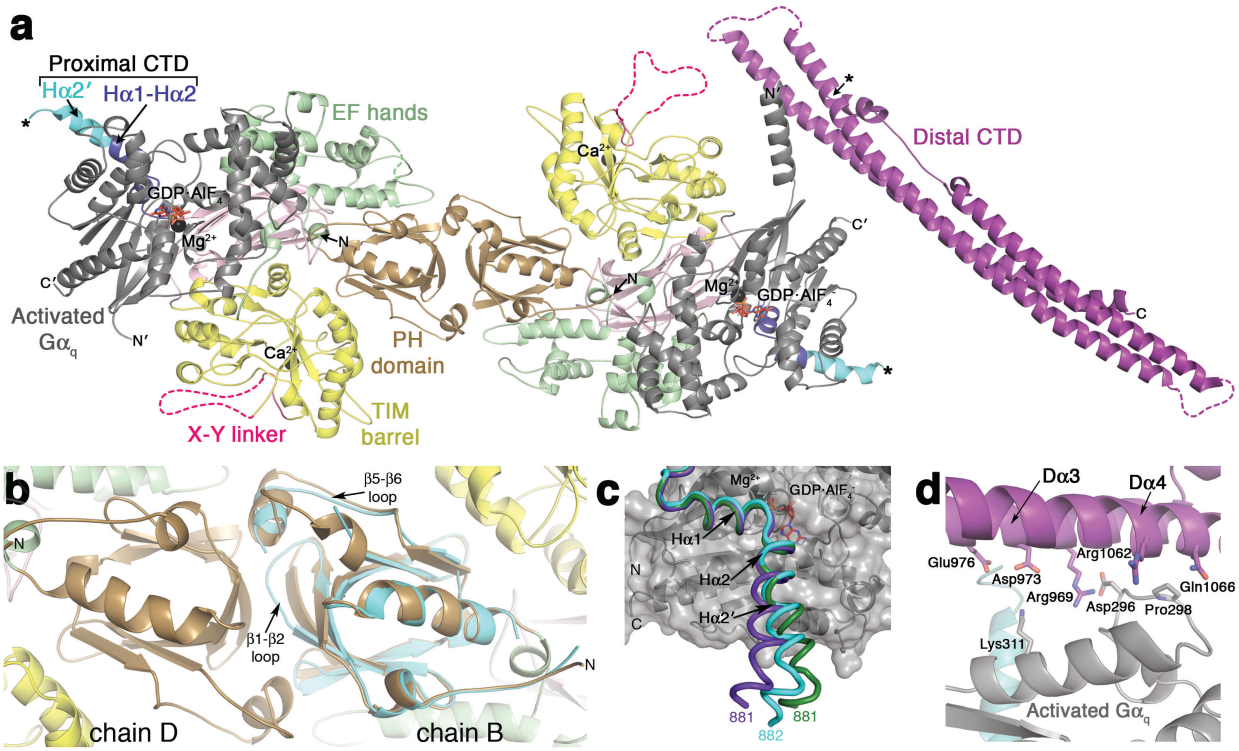

Supplementary Figure 2. Complete asymmetric unit of the $G\alpha_q$–PLCβ3 complex and identification of regions of special interest. PLCβ3 domains are colored as in **Fig. 1a**. (**a**) The $G\alpha_q$–PLCβ3 complex crystallized as a dimer mediated by the PH domain, in which the buried accessible surface area (~2000 $Å^2$) is comparable to that buried between the PH domain and Rac1 in the Rac1–PLCβ2 structure (~1200 $Å^2$)[43]. The C-terminus of the proximal CTDs and the N-terminus of the distal CTD are marked with black asterisks. The observed N- and C-termini of PLCβ3 and $G\alpha_q$ are labeled N and C, and N' and C', respectively. Ca^{2+} and Mg^{2+} are shown as black spheres. Disordered regions are marked as dashed lines. (**b**) The PH domains in the $G\alpha_q$–PLCβ3 structure form a dimer interface that differs in conformation from the PH domain in 3OHM (cyan)[18], most notably in the β1-β2 and β5-β6 loops. (**c**) The Hα2' helix, which binds to the PLCβ3 catalytic core in crystal contacts, is independently flexible with respect to the rest of the proximal CTD. Hα2' from 3OHM is shown as a cyan tube, and those from the B and D chains of the $G\alpha_q$–PLCβ3 structure as purple and green, respectively. The last observed residue in Hα2' is indicated. (**d**) The PLCβ3 distal CTD interaction with the Ras-like domain of $G\alpha_q$.

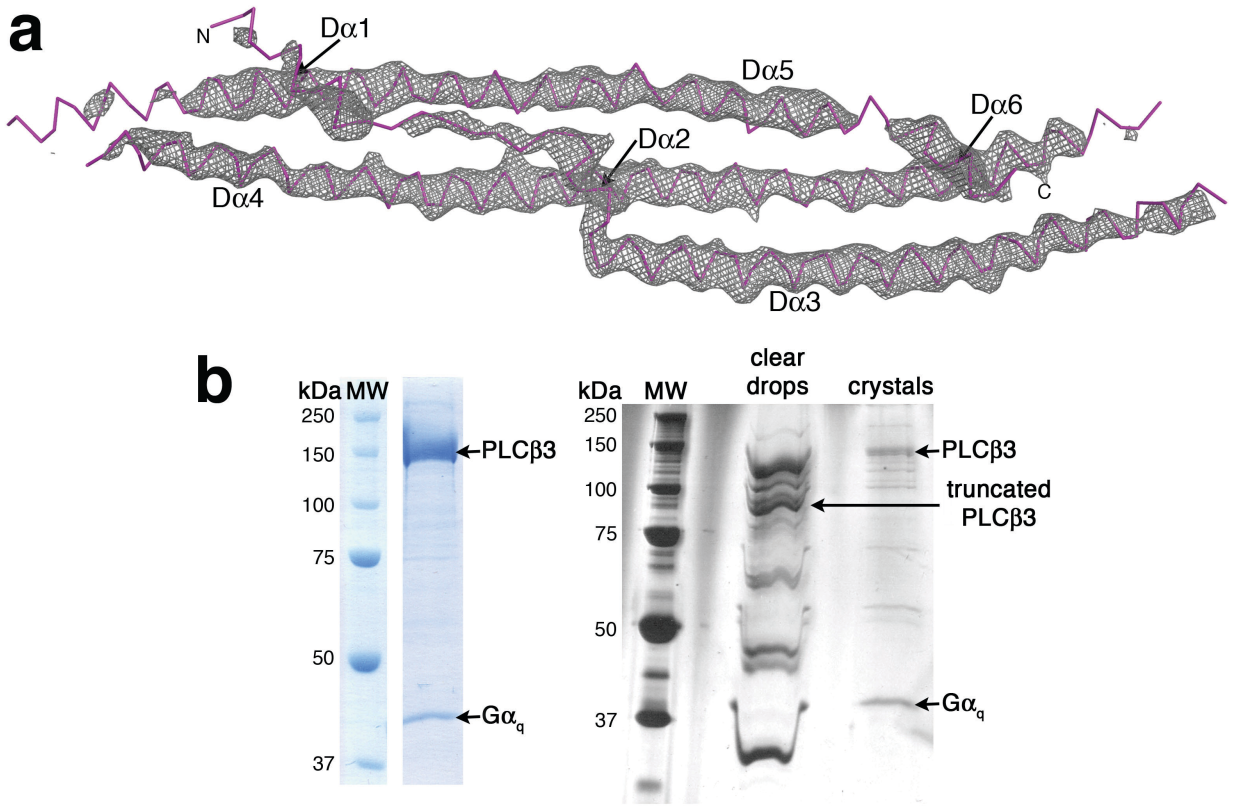

Supplementary Figure 3. Crystals of Gα$_q$–PLCβ3 contain full-length PLCβ3. (**a**) Strong electron density is observed for the backbone of the distal CTD. An m|F_o|–D|F_c| omit map contoured at 3 σ for the distal CTD is shown as a gray cage. This view is similar to that shown in **Fig. 2a**. (**b**) SDS-PAGE analysis of Gα$_q$–PLCβ3 isolated by gel filtration, stained with Coomassie blue (left), and from crystals, silver-stained (right). Crystals were harvested and dissolved in SDS loading dye prior to loading on a 10% acrylamide gel. Hanging drops without crystals were harvested as controls ("clear drops"). The high concentration of PEG 3350 and sodium chloride in the hanging drops alter the rate of protein migration. MW, molecular weight markers.

a

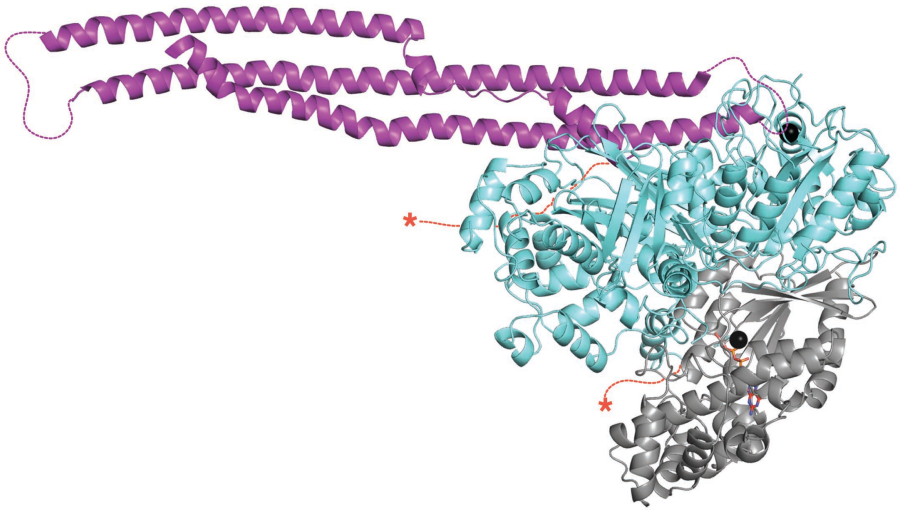

b

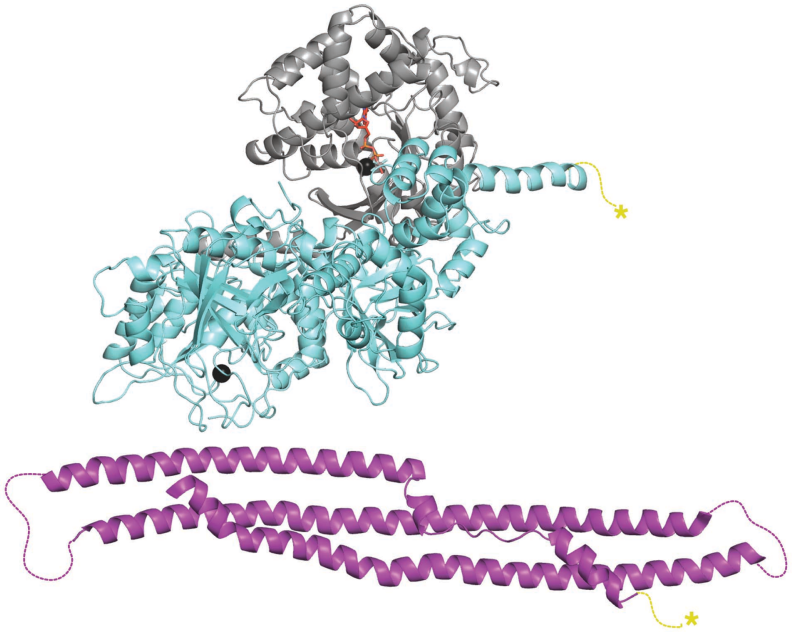

c

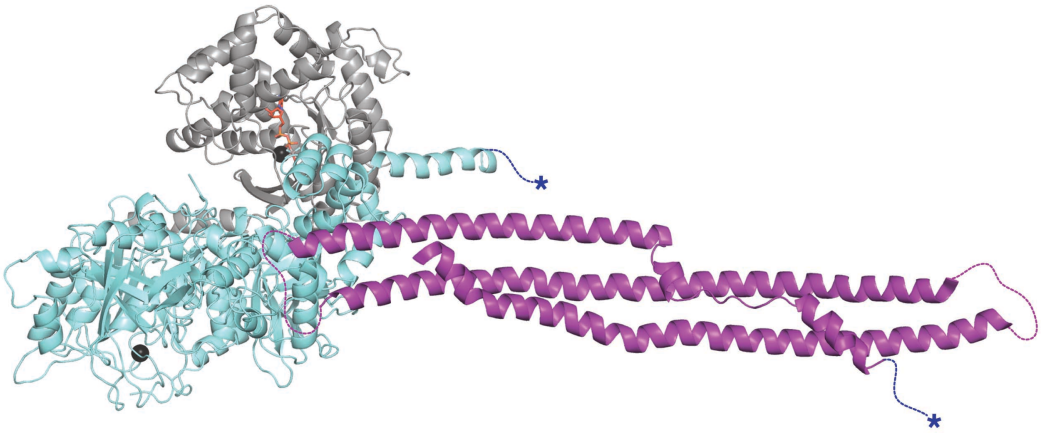

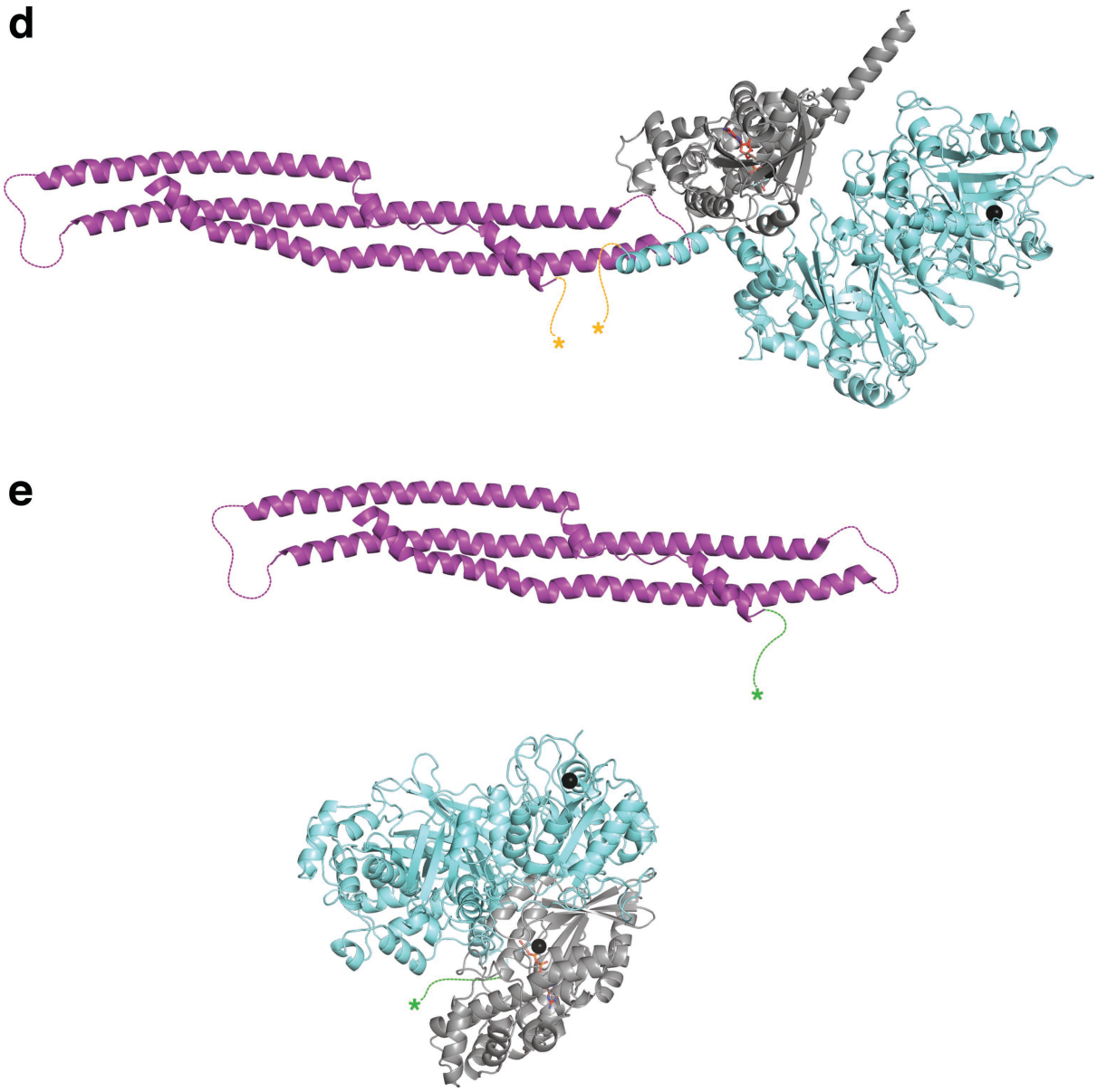

Supplementary Figure 4. Examples of possible PLCβ3 core linkages with the distal CTD within the crystal lattice. The CTD linker is conformationally flexible, and it is unclear which PLCβ3 core and distal CTD are covalently attached in the crystal lattice. Considering the length of the disordered linker (52 residues), there are many different combinations possible. Here we show only catalytic cores immediately adjacent to the distal CTD, which is drawn in the same orientation in each panel. These combinations are in addition to those shown in **Fig. 4**, which are configurations confirmed by cryo-EM. Activated $G\alpha_q$ is shown in gray, the GDP and AlF_4^- as red sticks, and the Mg^{2+} ion as a black sphere. The PLCβ3 core is shown in cyan with the catalytic calcium ion as a black sphere. The distal CTD is shown in purple and the C-terminus is labeled. The C-terminus of the proximal CTD and the N-terminus of the distal CTD of each pair are marked by asterisks.

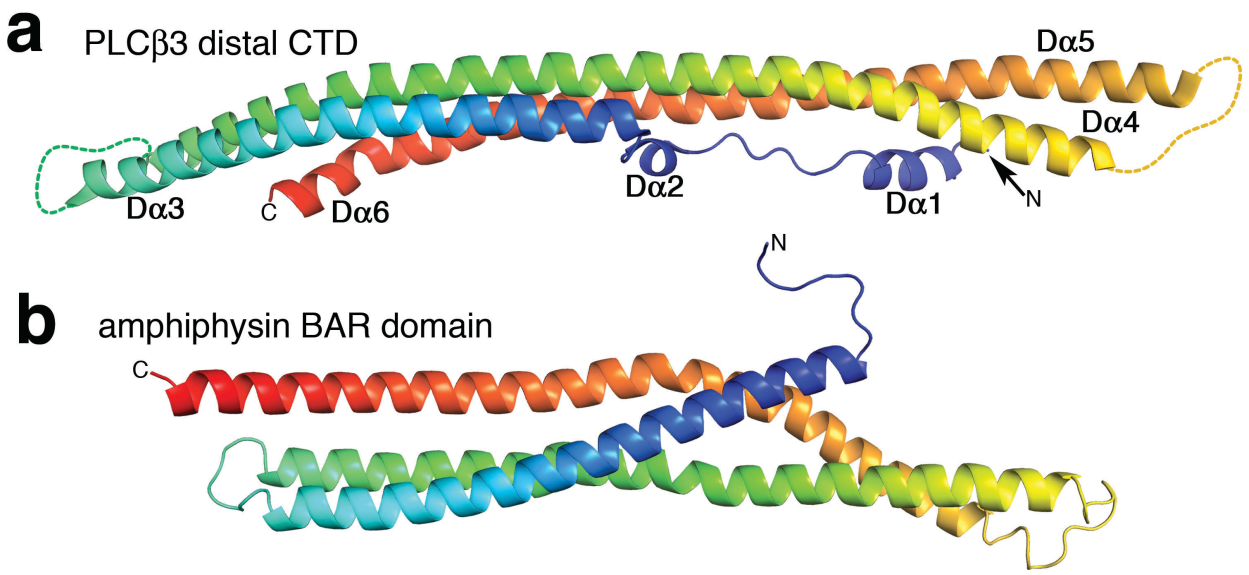

Supplementary Figure 5. The PLCβ3 distal CTD and BAR domains are coiled coils with similar shape and topology. Both structures are viewed towards their putative membrane binding surfaces. Structural alignment was performed using PyMOL. (**a**) The PLCβ3 distal CTD, colored in a ramp from blue at the N-terminus to red at the C-terminus. (**b**) Monomer of the amphiphysin BAR domain from *D. melanogaster* (PDB entry 1URU)[35]. The three core helices of the distal CTD and BAR domains (cyan to orange colored regions) adopt a similar fold, but the N- and C-terminal "arms" (blue and red regions, respectively) pack on opposite sides of the domain.

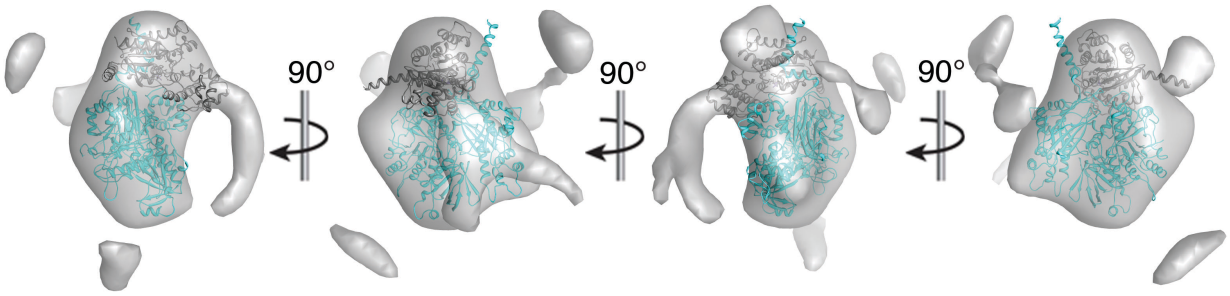

Supplementary Figure 6. Preliminary cryo-EM 3D reconstruction of the $G\alpha_q$–PLCβ3 complex. 40,124 particle projections were used to calculate a 3D reconstruction using the $G\alpha_q$–PLCβ3 core complex excluding the distal CTD as an initial reference volume. The map has poor definition and reveals several densities peripheral to the $G\alpha_q$–PLCβ3 core, but no clear location for the distal CTD.

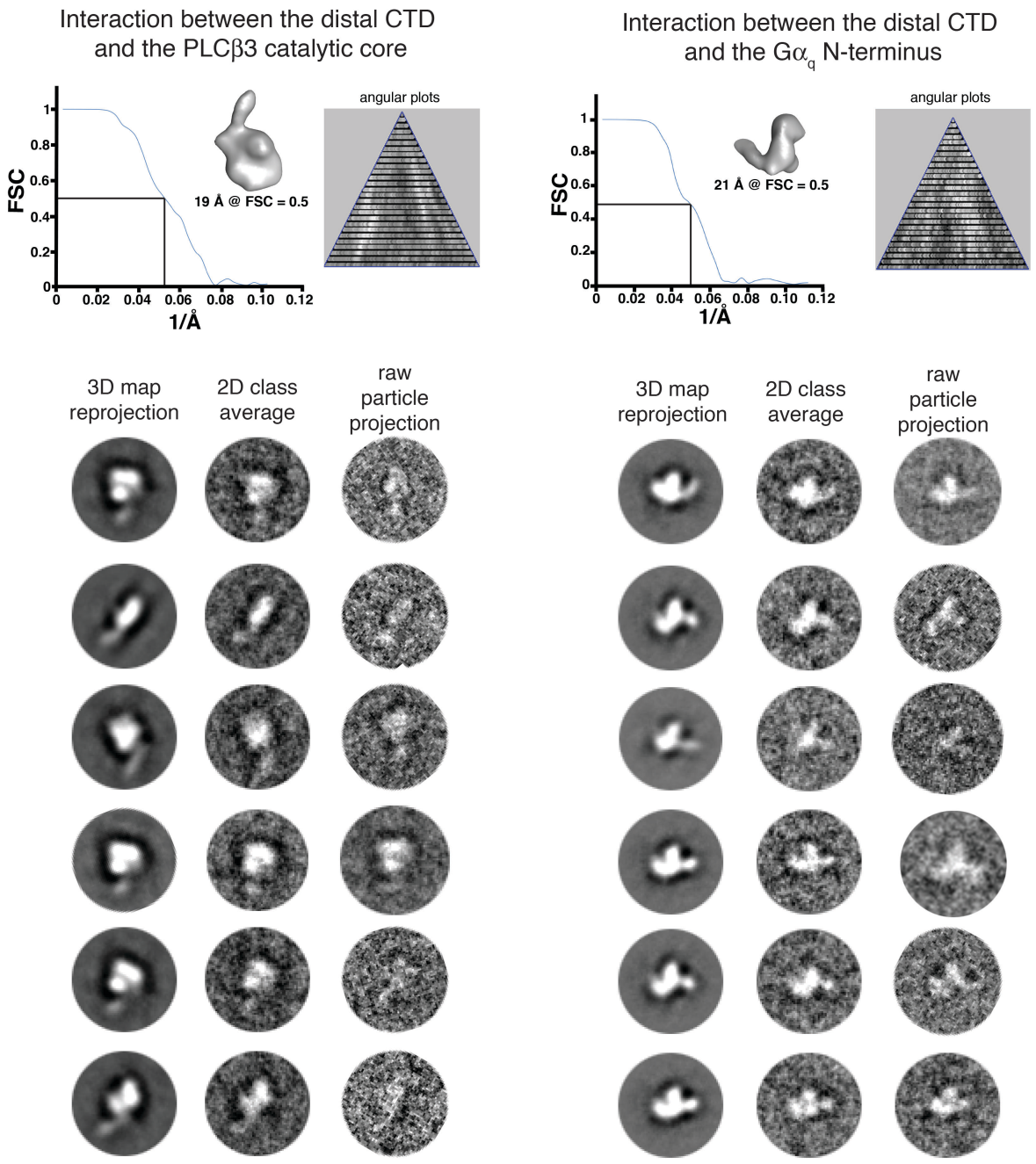

Supplementary Figure 7. Fourier shell correlation (FSC), angular distribution, and projection comparison for 3D reconstructions of the Gα$_q$–PLCβ3 complex. The FSC curve and angular distribution of particle projections reflecting the interaction between the distal CTD and the N-terminal helix of Gα$_{q.}$ (**a**) and interaction between the distal CTD and the PLCβ3 catalytic core (**b**). (**c**) Comparison of the 3D map reprojections, 2D class averages and raw particle projections for the distal CTD–Gα$_q$ N-terminal helix interface (left) and the (**d**) distal CTD–PLCβ3 catalytic core interface (right).

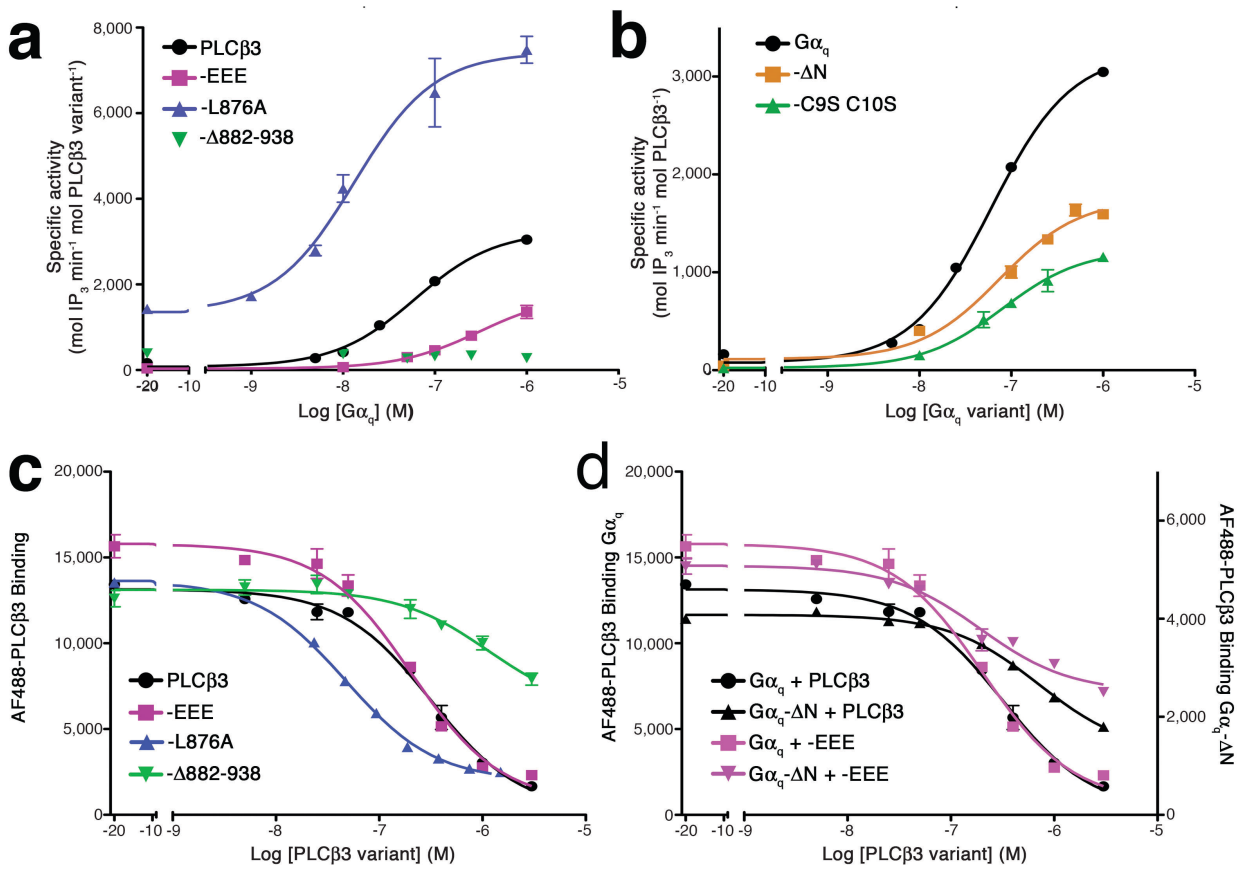

Supplementary Figure 8. Representative activation and competition binding curves. (**a**) $G\alpha_q$-stimulated activation of PLCβ3 variants. The activity of PLCβ3 and variants in the presence of increasing amounts of GDP·AlF_4^--activated $G\alpha_q$ was determined by measuring the amount of free [^{3}H]-IP_3 released from [^{3}H]-PIP_2-containing liposomes after 5 min at 30 °C. PLCβ3 (black circles), PLCβ3 L876A (blue triangles), and PLCβ3 EEE (dark pink squares) show robust $G\alpha_q$-stimulated activation. PLCβ3-Δ882–938 (green inverted triangles) was unresponsive to $G\alpha_q$ at all concentrations tested. (**b**) Activation of PLCβ3 by $G\alpha_q$ variants. Representative activation curves for PLCβ3 activation by $G\alpha_q$ (black circles), $G\alpha_q$-ΔN (orange squares), and $G\alpha_q$ C9S C10S (green triangles) are shown. All show similar EC_{50} values, but differ in their maximum specific activity. Due to difficulty in obtaining sufficient quantities of $G\alpha_q$ variants, not all curves in (a) or (b) could be measured to saturation, thus introducing some uncertainty in determination of their midpoints. (**c**) $G\alpha_q$ binding of PLCβ3 variants. A flow cytometry bead-based assay was used to quantify the ability the ability of PLCβ3 variants to displace an Alexa Fluor 488-labeled PLCβ3 variant (PLCβ3-Δ892 R9872A L876A L879A)[19] from biotinylated $G\alpha_q$ immobilized on streptavidin-coated beads. (**d**) The hydrophobic patch of the distal CTD does not contribute to high affinity binding. The ability of biotinylated $G\alpha_q$ or $G\alpha_q$-ΔN to bind PLCβ3 (black circles and black triangles, respectively) or PLCβ3 EEE (pink squares and pink inverted triangles, respectively) was measured in the same flow cytometry based binding assay. Whenever possible, variants in (c) and (d) that did not plateau at the highest concentration of PLCβ3 were run in the same experiment with variants that did (*e.g.* L876A) in order to establish the baseline and allow more accurate determination of IC_{50} values.

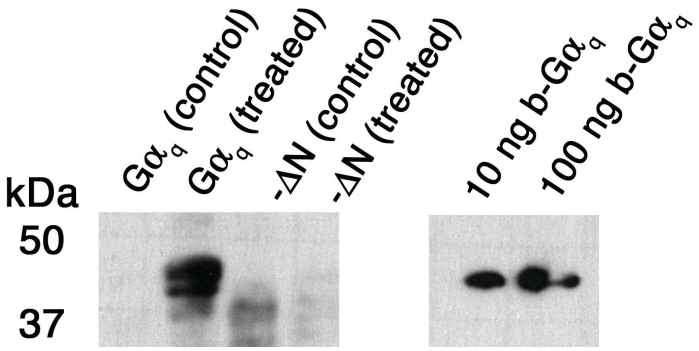

Supplementary Figure 9. Recombinantly expressed $G\alpha_q$ purified from the soluble fraction of High Five cells is at least partially palmitoylated. $G\alpha_q$ and $G\alpha_q$-ΔN were treated with N-ethylmaleimide to block free thiols, followed by buffer (control samples) or hydroxylamine (treated) to remove thiol-linked palmitoyl groups. All samples were then incubated with a biotin cross-linking reagent that conjugated to the newly exposed thiol groups. Protection of cysteines due to palmitoylation was detected by a western blot with a biotin antibody. Biotinylated $G\alpha_q$ (b-$G\alpha_q$) was used as a positive control.

SUPPLEMENTARY NOTE

Cryo-EM 3D Reconstructions. 40,124 particle projections from $G\alpha_q$–PLCβ3 images were interactively selected and excised using Boxer (EMAN 1.9 software suite)[51]. The CTF parameters for each micrograph were determined using *ctfit,* and CTF correction was applied accordingly using the program *Applyctf* (EMAN 1.9 software suite). In a first test, the full dataset of projections was used to determine a 3D reconstruction by projection matching in EMAN 1.9 using the structure of the $G\alpha_q$–PLCβ3 core complex without the distal CTD as an initial reference. The resulting 3D map showed no clear density attributed to the distal CTD, but revealed significant peripheral density at various positions around the core complex (**Supplementary Fig. 6**). To probe the conformational heterogeneity in particle population, we subjected the particle projections to classification by the maximum likelihood approach as implemented in XMIPP[58,59]. However, this approach was unsuccessful, perhaps due to the multiple distinct conformations adopted by the distal CTD with respect to the $G\alpha_q$–PLCβ3 core structure.

We then proceeded with multiple 3D reference-supervised classification by subjecting the full dataset to the "*multirefine*" routine[60,61] in EMAN 1.9 using as references 20 Å-filtered volumes of four possible models of the complex as observed in the crystal lattice (**Fig. 3**). In this way, four categories of particle projections were obtained according to maximum cross-correlation with the reprojections of the four crystal structure references. The total number of particles observed in each category is provided in **Fig. 3**.

In the next step, we used the unique particle datasets to calculate four independent 3D reconstructions using the same initial reference of the $G\alpha_q$–PLCβ3 core but without the distal

CTD, thus simultaneously eliminating model bias for the distal CTD position and testing the validity of the classification (**Fig. 3**). Only two of the four reconstructions, each stemming from over 30% of the total dataset, showed very good definition for the shape of the $G\alpha_q$–PLCβ3 core complex as well as additional significant elongated density attached to either $G\alpha_q$ or the PLCβ3 core. The agreement between these non-biased (for the CTD) reconstructions and the corresponding reference models we used initially during multiple-reference supervised classification confirms the validity of the methodology. Fourier shell correlation plots indicate that the two maps have resolutions of 19 and 21 Å (at FSC=0.5) for the interaction between the distal CTD and the $G\alpha_q$ N-terminal helix, and between distal CTD and the PLCβ3 core, respectively. Angular distribution plots for each reconstruction show a good coverage of Euler angles and there is a good agreement between the reprojections of each map, 2D class averages used for reconstruction, and raw particle projections (**Supplementary Fig. 7**).

SUPPLEMENTARY NOTE REFERENCES

58. Marabini, R. *et al*. Xmipp: an image processing package for electron microscopy. *J Struct Biol* **116**, 237-40 (1996).

59. Scheres, S.H., Nunez-Ramirez, R., Sorzano, C.O., Carazo, J.M. & Marabini, R. Image processing for electron microscopy single-particle analysis using XMIPP. *Nat Protoc* **3**, 977-90 (2008).

60. Brink, J. *et al*. Experimental verification of conformational variation of human fatty acid synthase as predicted by normal mode analysis. *Structure* **12**, 185-91 (2004).

61. Menetret, J.F. *et al*. Architecture of the ribosome-channel complex derived from native membranes. *J Mol Biol* **348**, 445-57 (2005).